(Received 23 March 2026, Accepted 29 April 2026, Scheduled 8 May 2026)

Multi-Objective Hierarchical Optimization Design of a Variable-Leakage-Flux Reverse-Pole Permanent Magnet Synchronous Motor with Vibration and Noise Suppression

Xiping Liu[1,2], Qianli Jia[1], Hongzhan Hu[1], Zhangqi Liu[1,2,*], Zhiguo Zhu[1], and Jiao Guo[1]

[1] *School of Electrical Engineering and Automation, Jiangxi University of Science and Technology, Ganzhou 341000, Jiangxi, China*
[2] *Gannan Laboratory, Ganzhou 341000, China*

ABSTRACT: To address the issue of significant fluctuations in radial electromagnetic forces in variable-leakage-flux reverse-salient-pole permanent magnet synchronous motors (VLF-RSPMs), which make stable operation at high speeds difficult, this paper combines an analysis of existing VLF-RSPMs with a novel optimization method to propose a multi-objective hierarchical optimization design method for VLF-RSPMs, which incorporates vibration and noise suppression. First, the paper analyzes the radial electromagnetic force model, natural frequencies, and electromagnetic vibration model of the VLF-RSPM. Second, based on the optimization objective of vibration and noise suppression, parameters with high sensitivity are optimized first through sensitivity analysis. Subsequently, the modal characteristics, radial electromagnetic forces, noise, and stress of the optimized VLF-RSPM are analyzed in detail. Finally, an experimental VLF-RSPM prototype and a test platform for measuring radial electromagnetic force fluctuations are designed. The results demonstrate that the multi-objective hierarchical optimization design method ensures the operational reliability of the optimized VLF-RSPM, enabling it to meet the requirements for high-speed operation.

1. INTRODUCTION

In recent years, variable-leakage-flux reverse-salient-pole permanent magnet synchronous motors (VLF-RSPMs) have been widely adopted in electric vehicles and renewable energy generation owing to their advantages, including high efficiency under weak-field operation, high torque across all operating conditions, and low torque ripple [1, 2]. However, to achieve the reverse-salient-pole characteristic, VLF-RSPM incorporates a magnetic barrier on the q-axis, which exacerbates motor vibration and noise; simultaneously, due to significant fluctuations in radial electromagnetic forces, the motor struggles to operate stably at high speeds, contradicting the original design intent of achieving a wide speed range through variable leakage flux. Consequently, suppressing electromagnetic vibration and noise caused by radial electromagnetic force fluctuations have become a hot topic of research among scholars [3–5].

Currently, the calculation methods for radial electromagnetic force waves primarily include analytical and numerical approaches. The analytical method utilizes Maxwell's stress tensor to derive an analytical expression for radial electromagnetic force waves from the air gap magnetic flux density equation [6]. Refs. [7–9] performed analytical calculations of radial electromagnetic force waves for built-in permanent magnet motor rotors with spoke-type, U-type, and V-type structures, respectively, while accounting for the effects of core saturation, thereby achieving accurate predictions of the motor's electromagnetic performance and physical fields. Ref. [10] presents an analytical model for the air-gap magnetic flux density of an IPMSM that neglects the effects of stator slotting and core saturation. By introducing a virtual rotor magnetic field and complex relative permeability to correct the calculation results, the model improves computational accuracy. It is evident that analytical methods ensure high computational accuracy and are widely used in calculating the air-gap magnetic flux density of permanent magnet motors; however, because analytical methods struggle to account for core saturation, complex structures, and losses, and make numerous simplifying assumptions regarding the magnetic field, core saturation, and slot effects, they lack general applicability and yield significant errors under complex operating conditions.

Among numerical methods, the finite element method (FEM) is the most widely used and serves as the mainstream solution method for electromagnetic force waves and electromagnetic vibration analysis. When calculating radial electromagnetic force waves using the finite element method, the analysis is based on electromagnetic field calculations, with the radial electromagnetic force waves solved using the Maxwell stress tensor method or the virtual work method [11, 12]. Ref. [13] established two multiphysics finite element analysis models based on the modal superposition method to investigate their vibration characteristics. Ref. [14] combined analytical methods with multiphysics coupled finite element analysis to propose a Fourier-based vibration model that balances accuracy and speed, thereby more precisely characterizing the non-ideal orthogonality between electromagnetic forces and modes.

* Corresponding author: Zhangqi Liu (liuzhq@jxust.edu.cn).

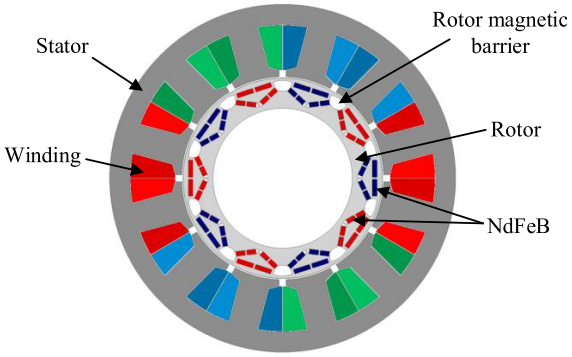

FIGURE 1. Motor topology of the VLF-RSPM.

As the number of multiphysics optimization objectives and parameters in motors increases, traditional optimization methods often fail to meet the constraints, necessitating the development of novel optimization methods [15, 16]. Ref. [17] employs the NSGA-II algorithm to perform multi-objective optimization of output torque and torque ripple. Ref. [18] categorizes motor structural parameters into multiple levels based on sensitivity analysis and selects high-sensitivity parameters for separate optimization. Ref. [19] established a mathematical model of the motor's nonlinear complex parameters and combined orthogonal experimental design with an improved non-dominant sorting genetic algorithm to perform phased optimization of the motor design, thereby achieving multi-objective optimization of highly sensitive parameters in permanent magnet motors.

In summary, to reduce the vibration and noise of the VLF-RSPM, this paper proposes a VLF-RSPM design that integrates parameter sensitivity-based hierarchical multi-objective optimization. This paper is organized as follows: First, a theoretical analysis of the motor's vibration noise is conducted, and a finite element model of the VLF-RSPM is constructed; second, a hierarchical collaborative optimization method is applied to the topological structure parameters; then, the optimized motor structure is simulated in a multiphysics environment to analyze vibration and noise performance; finally, the stability of the motor structure is verified in the multiphysics environment, and the accuracy of the model is validated through experiments.

2. VLF-RSPM TOPOLOGY AND VIBRATION-NOISE PRINCIPLES

2.1. VLF-RSPM Topology

In this paper, a motor model, as shown in Figure 1, is developed using Maxwell software. This VLF-RSPM achieves torque enhancement by connecting a single-row permanent magnet and a V-shaped permanent magnet in series; simultaneously, a magnetic barrier is designed along the q-axis to achieve variable leakage flux characteristics. Specific structural parameters are listed in Table 1.

TABLE 1. VLF-RSPM structural parameters.

Items	VLF-RSPM
Rated output power (kW)	4
Rated Current (A)	10
Air-gap length (mm)	0.7
Rated speed (rpm)	1500
Out diameter of stator (mm)	155
Out diameter of rotor (mm)	89.2
Permanent magnet materials	N42SH

2.2. Air-Gap Magnetic Flux Density

This paper employs the magnetic potential-permeability method to calculate the air-gap magnetic flux density in a VLF-RSPM. The radial air-gap magnetic flux density in a VLF-RSPM is determined by the air-gap permeability and the total magnetic potential, and the basic expression is [20]:

$$B_r(\theta,t) = \lambda(\theta,t) \cdot f_\Sigma(\theta,t) \tag{1}$$

where θ is the mechanical angle; t is the time; m is the number of phases of the motor; $B(\theta,t)$ represents the radial air-gap magnetic flux density; $\lambda(\theta,t)$ represents the air-gap permeability; and $f_\Sigma(\theta,t)$ represents the total magnetic field force, which is the superposition of the rotor magnetic field force ($f_r(\theta,t)$), the stator magnetic field force ($f_s(\theta,t)$), and the DC excitation magnetic field force of the annular excitation winding, that is:

$$f_\sum(\theta,t) = f_r(\theta,t) + f_s(\theta,t) + C \tag{2}$$

The magnetic potential is the source of the magnetic field. The rotor and stator magnetic potentials take the form of space-time harmonics, while the DC excitation magnetic potential is constant. The relationship between the magnetic potential of the air-gap flux density and the magnetic potentials of the stator and permanent magnets is as follows:

$$\begin{cases} f_r(\theta,t) = \sum\limits_{\mu} F_{r\mu}\cos(\mu p\theta - \mu\omega_1 t) \\ f_s(\theta,t) = \sum\limits_{\nu} F_{s\nu}\cos(\nu p\theta - n\omega_1 t) \\ C = constant \end{cases} \tag{3}$$

where $\mu = 2i+1\,(i = 0,1,2,...)$ represents the odd-order harmonic of the rotor magnetic field; $v = 2mj + n\,(j = 0,\pm1,\pm2,...)$ represents the harmonic of the stator magnetic field; $F_{r\mu}$ and F_{sv} are the amplitudes of the μ and v harmonic of the rotor and stator magnetic field, respectively; p is the number of pole pairs of the motor; ω_1 is the electrical angular velocity; n is the harmonic order of the armature current.

In the VLF-RSPM, slots are only cut into the stator surface; the tooth-slot effect causes the air-gap permeability to exhibit a periodic harmonic distribution, and its permeability is expressed as:

$$\lambda(\theta,t) = \Lambda_0 + \sum_{k_s} \Lambda_{sk}\cos(k_s Z_s\theta) \tag{4}$$

where Λ_0 is the average permeability; Λ_{sk} is the amplitude of the kth harmonic of the stator permeability ($k = 1,2,3,...$); Z_s is the number of stator slots; and $k_s Z_s$ is the spatial order of the permeability.

TABLE 2. Spatial and frequency order of VLF-RSPM radial force waves.

No.	Source	Spatial order	Frequency order
1	Permanent magnetic field	$(\mu_1 \pm \mu_2) \cdot p$	$(\mu_1 \pm \mu_2) \cdot f$
2	Interaction between the permanent magnet field and the stator slots	$(\mu_1 \pm \mu_2) \cdot p \pm kz$ $(\mu_1 \pm \mu_2) \cdot p \pm (k_1 \pm k_2)z$	$(\mu_1 \pm \mu_2) \cdot f$
3	Interaction between the permanent magnet field and the armature field	$(\mu \pm v) \cdot p$	$(\mu \pm n) \cdot f$
4	Interaction between the permanent magnet field, stator slots, and the armature magnetic field	$(\mu \pm v) \cdot p \pm kz$ $(\mu \pm v) \cdot p \pm (k_1 \pm k_2)z$	$(\mu \pm n) \cdot f$
5	Armature magnetic field	$(v_1 \pm v_2) \cdot p$	$(n_1 \pm n_2) \cdot f$
6	Interaction between the armature magnetic field and the stator slots	$(v_1 \pm v_2) \cdot p \pm kz$ $(v_1 \pm v_2) \cdot p \pm (k_1 + k_2)z$	$(n_1 \pm n_2) \cdot f$

Substituting Equations (2), (3), and (4) into Equation (1) and expanding yields the air-gap magnetic flux density of the VLF-RSPM as:

$$\begin{aligned} B_r(\theta,t) &= \left[\Lambda_0 + \sum_{k_s} \Lambda_{sk} \cos(k_s Z_s \theta)\right] \\ &\cdot \left[\sum_{\mu} F_{r\mu} \cos(\mu p\theta - \mu\omega_1 t)\right. \\ &\left. + \sum_{v} F_{sv} \cos(vp\theta - n\omega_1 t) + C\right] \end{aligned} \tag{5}$$

2.3. Radial Electromagnetic Force

Radial electromagnetic force waves are the primary source of electromagnetic vibration in electric motors. In this paper, the square term of the radial magnetic flux density is expanded using the Maxwell stress tensor method to derive the harmonic components of the force waves. In the air gap of an electric motor, assuming that the tangential magnetic flux density is negligible and the ferromagnetic material is nonlinear, the fundamental expression for the radial electromagnetic force wave is:

$$F_r(\theta,t) = \frac{B_r^2(\theta,t)}{2\mu_0} \tag{6}$$

where μ_0 is the magnetic permeability of free space, and $F_r(\theta,t)$ is the spatiotemporal distribution of the radial electromagnetic force wave.

Substituting Equation (5) into Equation (6) and expanding using the quadratic formula yields a six-term expansion of the radial electromagnetic force wave:

$$\begin{aligned} F_r(\theta,t) &= \frac{B_r^2}{2\mu_0} = \frac{\left[f_r(\theta,t) + f_s(\theta,t) + C\right]^2 \lambda^2(\theta)}{2\mu_0} = \frac{1}{2\mu_0} \\ &\cdot \left[\sum_{\mu} F_{r\mu} \cos(\mu p\theta - \mu\omega_1 t) + \sum_{v} F_{sv} \cos(vp\theta - n\omega_1 t) + C\right]^2 \\ &\cdot \left[\Lambda_0 + \sum_{k_s} \Lambda_{sk} \cos(k_s Z_s \theta)\right]^2 \\ &= \underbrace{\frac{\lambda(\theta,t)^2 f_r(\theta,t)^2}{2\mu_0}}_{\text{Permanent magnetic field}} + \underbrace{\frac{f_r(\theta,t)^2 \sum_k \lambda_k \cos(kZ_s\theta)}{2\mu_0}}_{\text{Interaction between the permanent magnet field and the stator slots}} \\ &+ \underbrace{\frac{\lambda(\theta,t)^2 f_r(\theta,t) f_s(\theta,t)}{\mu_0}}_{\text{Interaction between the permanent magnet field and the armature field}} + \underbrace{\frac{f_r(\theta,t) f_s(\theta,t) \sum_k \lambda_k \cos(kZ_s\theta)}{\mu_0}}_{\text{Interaction between the permanent magnet field, stator slots, and the armature magnetic field}} \\ &+ \underbrace{\frac{\lambda(\theta,t)^2 f_s(\theta,t)^2}{2\mu_0}}_{\text{Armature magnetic field}} + \underbrace{\frac{f_s(\theta,t)^2 \sum_k \lambda_k \cos(kZ_s\theta)}{2\mu_0}}_{\text{Interaction between the armature magnet field and the stator slots}} \\ &+ \underbrace{\frac{\left[C^2 + 2f_r(\theta,t)C + 2f_s(\theta,t)C\right]\lambda(\theta)^2}{2\mu_0}}_{\text{Non-vibrational DC component}} \end{aligned} \tag{7}$$

A two-dimensional discrete Fourier analysis was performed on the components of the radial electromagnetic force waves, while the alternating force wave components were separated from the non-vibrational DC components. This yielded the frequency and spatial orders of each force wave component, as shown in Table 2.

When C equals 0, there is no DC bias, and the force waves are generated solely by three components: the fundamental rotor magnetic field, the fundamental armature reaction magnetic

field, and the stator magnetic permeability tooth harmonics; all frequencies are even multiples; when C is not equal to 0, DC bias must be considered. In this case, the DC component of the air-gap magnetic flux density interacts with the odd-order harmonic magnetic flux density, generating low-order, high-amplitude force waves with odd-order harmonics, resulting in odd-order harmonic components in the frequency spectrum.

2.4. Stator Natural Frequencies of Electric Motors and Analysis of Their Electromagnetic Vibrations

The natural frequency of a stator is the frequency at which the stator vibrates freely without any external excitation; it is an inherent physical property of the stator structure. By calculating the stator's natural frequency and reducing the frequency of the electromagnetic force waves, the magnitude of electromagnetic vibrations can be effectively suppressed [21]. The zero-order (f_0), first-order (f_1), and higher-order (f_n) natural frequencies of the stator can be expressed as:

$$\begin{aligned} f_0 &= \frac{1}{\pi D_c}\sqrt{\frac{e}{\rho\Delta}} \\ f_1 &= f_0\sqrt{\frac{2}{1+i^2\frac{\Delta_n}{\Delta}}} \\ f_n &= f_0\frac{in(n^2-1)}{\sqrt{n^2+1}}\frac{1}{\sqrt{1+\frac{i^2(n^2-1)\left[n^2\left(4+\frac{\Delta_n}{\Delta}\right)+3\right]}{n^2+1}}} \end{aligned} \tag{8}$$

where D_c is the average diameter of the stator core; e is the Young's modulus of the stator core material; ρ is the density of the stator core material; Δ is the radial thickness of the stator core yoke; i is the axial mode order; and Δ_n is the equivalent radial thickness of the stator winding.

Ignoring the tangential magnetic flux density, when the motor is subjected to a radial electromagnetic force, the deformation of the stator can be expressed as:

$$D_s = \frac{F_r}{\left(M^2-1\right)^2}\cdot\frac{1}{1-\left(\frac{f_v}{f_c}\right)^2} \tag{9}$$

where D_s represents the deformation of the stator core; M represents the order of the radial electromagnetic force; f_v and f_c represent the electromagnetic vibration frequency and the motor's natural frequency, respectively.

Consequently, the lower-order natural frequencies of the stator — due to their lower frequencies and mode shapes that are more likely to achieve spatial and frequency matching with radial electromagnetic force waves — are more easily excited by these waves. When the frequency of the radial electromagnetic force wave is close to or matches a particular natural frequency of the stator, structural resonance is triggered, causing a sharp amplification of the deformation and vibration amplitude of the stator core.

2.5. Sound Pressure Level

The sound pressure level of motor noise is a core acoustic indicator used to quantitatively characterize the intensity of airborne noise emitted by a motor. By converting the effective sound pressure at a measurement point to a decibel value using a logarithmic scale, it provides an intuitive representation of the loudness level of motor noise and serves as a key parameter for motor noise testing, rating, and optimization. The sound pressure level of motor noise is expressed as

$$L_P = 20\lg\frac{P}{P_0} \tag{10}$$

where L_p represents the sound pressure level of the motor noise; P represents the effective sound pressure of the motor noise at the measurement point; and P_0 represents the reference sound pressure, i.e., $P_0 = 2\times10^{-5}$ Pa.

3. TOPOLOGICAL HIERARCHICAL OPTIMIZATION DESIGN

As the number of optimization objectives and parameters in motor multiphysics optimization increases, traditional optimization methods group all optimization parameters into a single category, which can lead to the neglect of parameter ranges with high sensitivity in order to reduce electromagnetic vibrations in VLF-RSPM. In this paper, incorporating the concept of hierarchical optimization, we first perform a sensitivity analysis on all parameters to be optimized. For highly sensitive parameters, we employ a motor topology co-optimization scheme, while for the remaining parameters, we use the traditional scanning method for optimization [18]. The flowchart of the VLF-RSPM co-optimization process is shown in Figure 2.

Based on the VLF-RSPM rotor topology shown in Figure 3, this paper selects the parameters depicted in the figure for sensitivity analysis and optimization. The specific design variables and their ranges are listed in Table 3.

3.1. Parameter Sensitivity Analysis Screening

To enhance the output torque capability of the VLF-RSPM while suppressing electromagnetic vibration noise caused by fluctuations in the radial electromagnetic force, this paper selects the following optimization objectives: average output torque (T_e), amplitude of the radial electromagnetic force (F_r), amplitude of stator vibration (V_s), and average noise sound pressure level (L_v).

Based on the parametric model of the VLF-RSPM shown in Figure 3, this paper employs sensitivity analysis to distinguish the specific influence of each variable on the optimization objectives. The sensitivity index expressions are as follows:

$$S(x_i) = \frac{D_i}{D} = \frac{V(E(F/x_i))}{V(F)} \tag{11}$$

Figure 4 shows the sensitivity plots of various parameter variables in the VLF-RSPM model with respect to T_e, F_r, V_s, and L_v. The circular scale ranging from -1 to 1 represents

TABLE 3. Design variables and variation ranges.

Design Variables	Introduction	Variation Ranges
θ (deg)	Angle of inclination of the V-shaped permanent magnet	[20–40]
T_{PM1} (mm)	Thickness of a single-piece permanent magnet	[1–3]
T_{PM2} (mm)	Thickness of V-shaped permanent magnets	[1–3]
W_{PM} (mm)	Width of V-shaped permanent magnet	[3–5]
W_{bri} (mm)	Magnetic bridge width	[0.5–2.5]
H_{PM} (mm)	Height from the V-shaped permanent magnet to the bottom of the rotor	[1–3]
R_B (mm)	Distance from the top of the magnetic barrier to the center	[43–44.5]
W_B (mm)	Magnetic barrier width	[3–5]
H_B (mm)	Magnetic barrier height	[3–6]

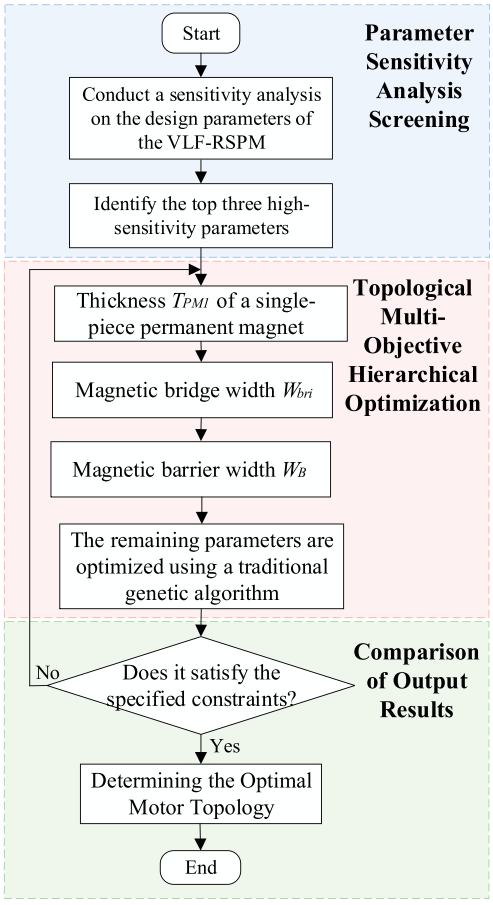

FIGURE 2. VLF-RSPM co-optimization flowchart.

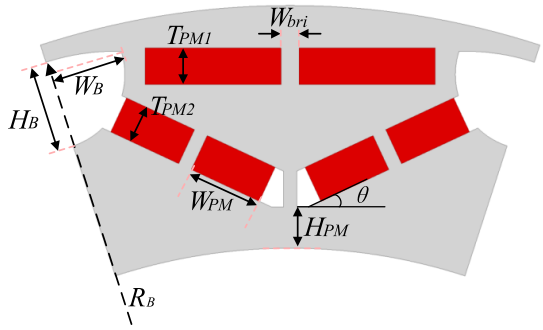

FIGURE 3. Motor topology of the VLF-RSPM.

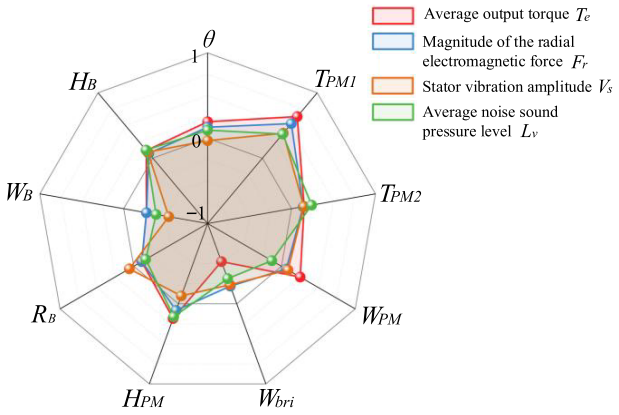

FIGURE 4. Sensitivity analysis of VLF-RSPM parameters.

normalized changes in performance. The farther a node corresponding to a parameter is from the center, the higher its value is, indicating that the parameter has higher sensitivity to that performance metric and a more significant impact on the optimization objective; conversely, a lower value indicates lower sensitivity and a weaker impact.

3.2. Topological Multi-Objective Hierarchical Optimization

Based on the parameter sensitivity analysis of the VLF-RSPM shown in Figure 4, since the absolute values of the sensitivity for the three parameters — thickness of the single-row permanent magnet (T_{PM1}), width of the magnetic bridge (W_{bri}), and width of the magnetic barrier (W_B) — are relatively high, these three parameters were selected for the motor topology co-optimization scheme.

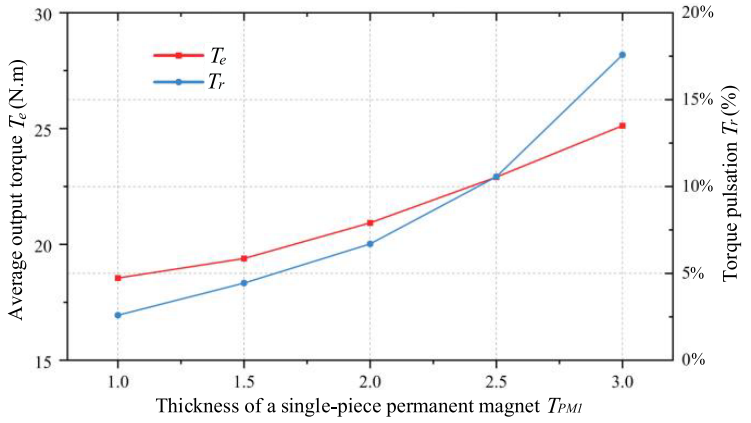

FIGURE 5. The relationship between T_{PMI} variables and motor electromagnetic torque and its fluctuations.

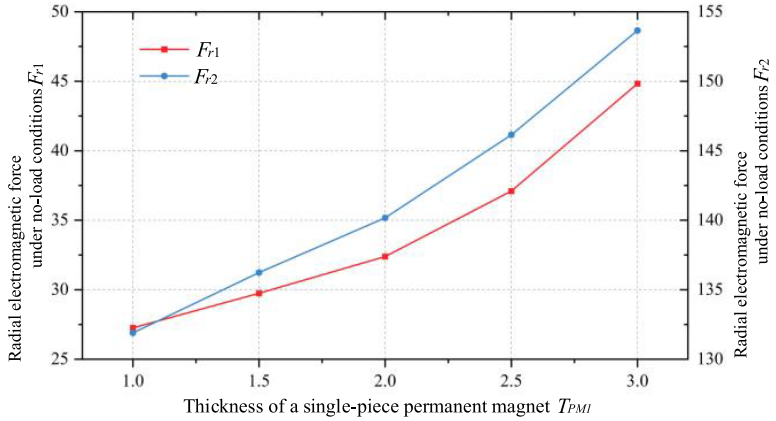

FIGURE 6. Relationship between the T_{PMI} variable and the radial electromagnetic force of the motor.

3.2.1. Analysis of the Thickness of a Single-Pole Permanent Magnet (T_{PMI})

First, the thickness of the rotor's linear permanent magnets (T_{PMI}) was optimized; the resulting electromagnetic torque and its ripple curve are shown in Figure 5. As T_{PMI} increased, the electromagnetic torque rose from 18.6 N·m to 25.1 N·m; torque ripple increased from 2.6% to 17.6%, representing a 15% increase. Since the increase in electromagnetic torque with T_{PMI} is relatively slow, but the torque ripple increases significantly, the range of T_{PMI} values can be narrowed. Ultimately, the optimal performance is achieved when T_{PMI} is set between 1.5 and 2.5. Since T_{PMI} exhibits the highest sensitivity to radial electromagnetic forces, an analysis of T_{PMI} was conducted to determine the relationship between the variable-leakage-flux motor and radial electromagnetic forces. As shown in Figure 6, the radial electromagnetic force shows a gradually increasing trend. Similarly, based on the torque output, T_{PMI} is set between 1.5 and 2.5.

3.2.2. Analysis of the Width of the Magnetic Bridge (W_{bri})

By segmenting the rotor's permanent magnets to form magnetic bridges, the path of the rotor's magnetic flux lines can be altered, thereby mitigating magnetic flux density oversaturation. However, excessive magnetic bridge width reduces magnetic flux density and lowers the output torque of the VLF-RSPM. Therefore, optimizing the magnetic bridge width (W_{bri}) aids in analyzing the stray flux phenomenon in variable-leakage-flux motors. Figure 7 shows the effects of T_{PMI} and W_{bri} on the electromagnetic torque and its ripple curve of the VLF-RSPM.

As shown in Figure 7(b), W_{bri} has a relatively minor effect on the torque ripple of the VLF-RSPM. As shown in Figure 7(a), when T_{PMI} increases and W_{bri} decreases, the electromagnetic torque of the VLF-RSPM significantly improves; however, as the electromagnetic torque increases, so does its ripple. As T_{PMI} increases, the torque ripple of the VLF-RSPM intensifies. Based on a comprehensive analysis of T_{PMI} and W_{bri}, $T_{PMI} = 2$ mm and $W_{bri} = 1$ mm were ultimately selected.

3.2.3. Analysis of the Width of the Magnetic Barrier (W_B)

Finally, the width of the magnetic barrier (W_B) is optimized. The magnetic barrier establishes a direct and close relationship with the radial electromagnetic force by regulating the distribution of the rotor magnetic circuit's leakage flux and the amplitude and harmonic characteristics of the air gap magnetic flux density. As the width of the magnetic barrier bridge in-

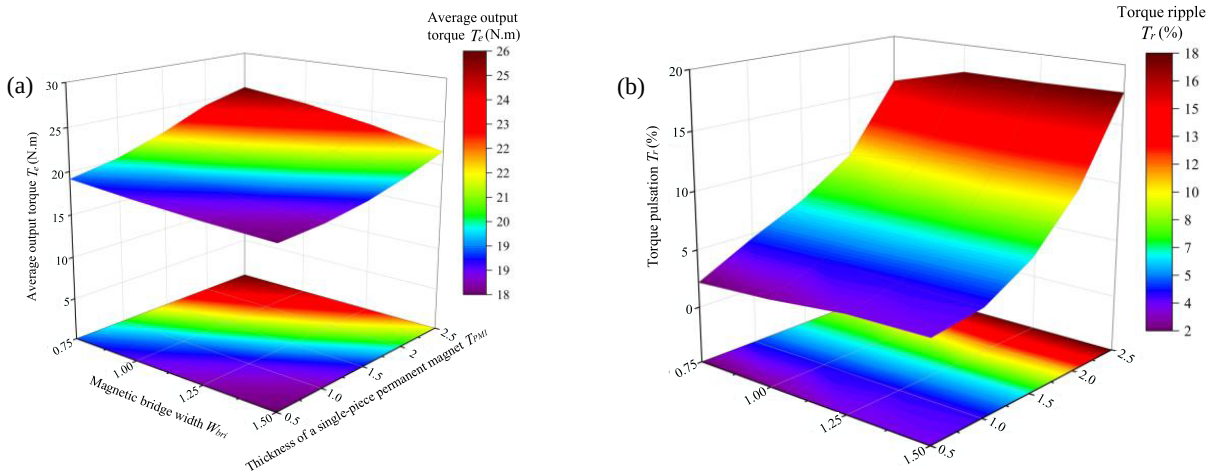

FIGURE 7. Analysis of the effects of T_{PMI} and W_{bri} on VLF-RSPM. (a) Electromagnetic torque. (b) Torque ripple.

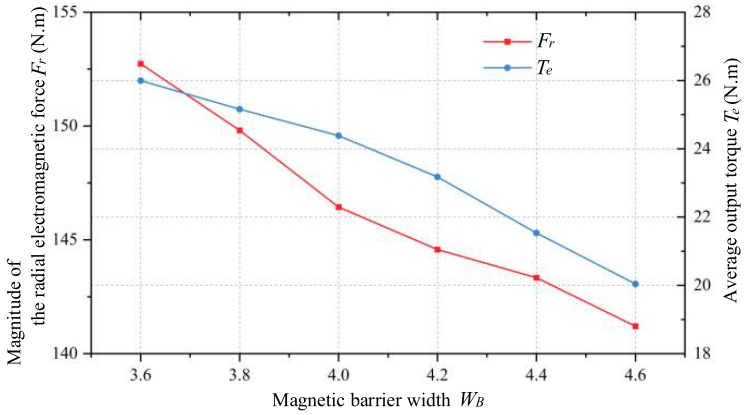

FIGURE 8. The relationship between W_B variables and the radial electromagnetic force and electromagnetic torque of the motor.

TABLE 4. Comparison of motor parameters and performance before and after optimization.

Design variables	Initial values	Optimized values
θ (deg)	30	25
T_{PMI} (mm)	2	2
T_{PM2} (mm)	2	2.1
W_{PM} (mm)	2	4.1
W_{bri} (mm)	2	1
H_{PM} (mm)	2	2.3
R_B (mm)	44	43.6
W_B (mm)	4	4.2
H_B (mm)	5	4.8
Average output torque (N·m)	26.4	26.2
Torque ripple (%)	12.5	7.6
No-load radial force magnitude (N·m)	45.3	39.1
No-load noise amplitude (dB)	82.3	75.3

creases, the rotor's leakage flux increases; the effective permanent magnet flux density decreases; and the amplitude of the air gap magnetic flux density consequently decreases. Based on the above analysis, when $T_{PMI} = 2$ mm and $W_{bri} = 1$ mm, the relationship between W_B and the radial force and electromagnetic torque of the VLF-RSPM is established, as shown in Figure 8.

As shown in Figure 8, as W_B increases, the radial electromagnetic force decreases from 152.7 N·m to 141.2 N·m, and the electromagnetic torque decreases from 25.9 N·m to 20.1 N·m. Since the rate of decrease in electromagnetic torque accelerates as W_B changes, while the rate of decrease in radial electromagnetic force slows down, W_B can be selected at 4.2 mm to achieve the optimal result.

After performing co-optimization of the motor topology using the above three parameters, the remaining parameters were optimized using the traditional scanning method, achieving results comparable to those of the co-optimization. The final values for each parameter are shown in Table 4.

4. MULTIPHYSICS ANALYSIS

The analysis of motor vibration and noise involves the coupling among electromagnetic, mechanical, and acoustic fields. To assess the accuracy of parameter-sensitive multi-objective hierarchical optimization, this section analyzes the multiphysics

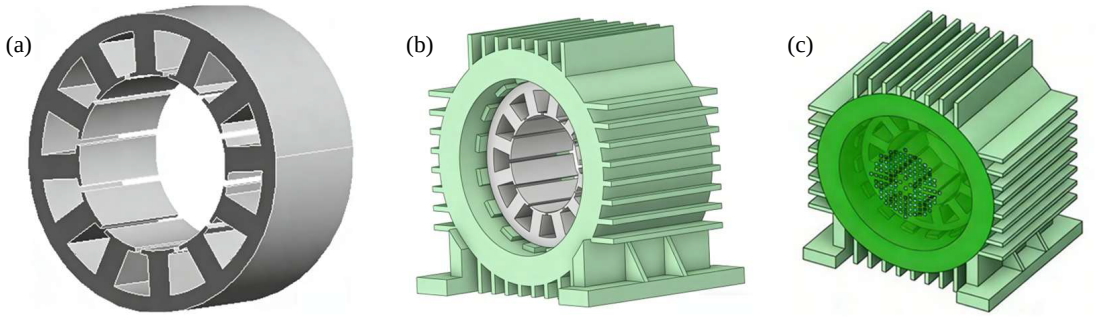

FIGURE 9. Modal analysis models of the VLF-RSPM: (a) Standalone stator model; (b) Combined model including the stator and housing; (c) Complete assembly model.

TABLE 5. Natural frequencies of the three models.

Model	Order	Natural frequency (Hz)					
		First-order	Second-order	Third-order	Fourth-order	Fifth-order	Sixth-order
standalone stator model	Modal	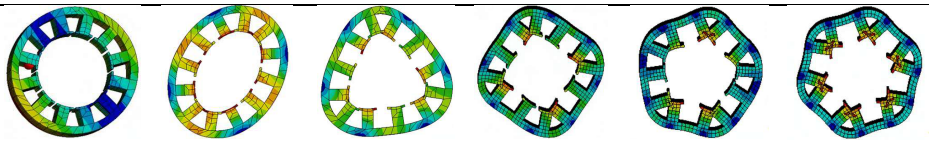					
	Frequency (Hz)	0	749.5	1942.3	3441.2	4713.3	5270.2
combined model including the stator and housing	Modal	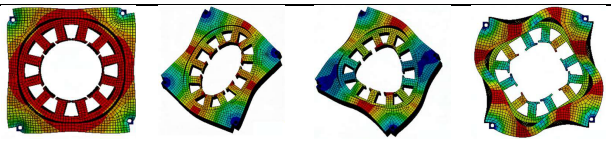					
	Frequency (Hz)	0	1002.8	1915.8	2785.3		
complete assembly model	Modal	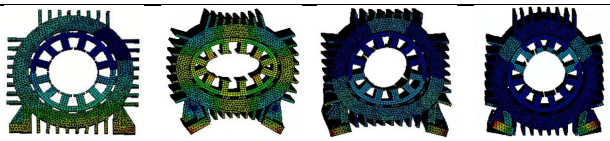					
	Frequency (Hz)	0	1866.6	2823.6	4490.7		

model of the VLF-RSPM and verifies the stability of the motor structure

4.1. Vibration Analysis

Based on the above analysis, this study will develop three different modal analysis models for the VLF-RSPM, including a standalone stator model, a combined model comprising the stator and housing, and a constrained full-machine model, as shown in Figure 9.

The frequencies of each order in the motor's modal analysis correspond to the motor's mechanical natural frequencies. The results of the motor's modal analysis are shown in Table 5. In the mechanical simulation, the motor stator was solved without any external constraints to determine the modal frequencies of each order.

The results of the modal analysis show that when the stator is assembled with the housing, its natural frequency increases compared to that of the stator alone; furthermore, the natural frequency rises even higher when the entire machine is assembled. For the complete machine model, the increase in natural frequency tends to level off as the modal order increases, indicating that the influence of individual components on the overall dynamic characteristics gradually weakens at higher modal orders. However, the natural frequencies of the complete machine at all orders remain significantly higher than the results obtained when considering only the stator or the stator-housing assembly. This phenomenon demonstrates that, when conducting research on the electromagnetic vibration and noise characteristics of electric motors, the coupling effects between structural components cannot be ignored and must be fully accounted for in modeling and analysis to ensure accurate assessment of vibration responses and noise sources.

The fundamental radial electromagnetic force generated by the interaction between the permanent magnet field and the fundamental armature reaction is the primary excitation source of motor vibration and noise under all operating conditions. The specific influence patterns of each harmonic order are as follows:

(1) Low-order radial electromagnetic force harmonics: Dominate vibrations under conventional operating conditions, such as no-load and rated load;

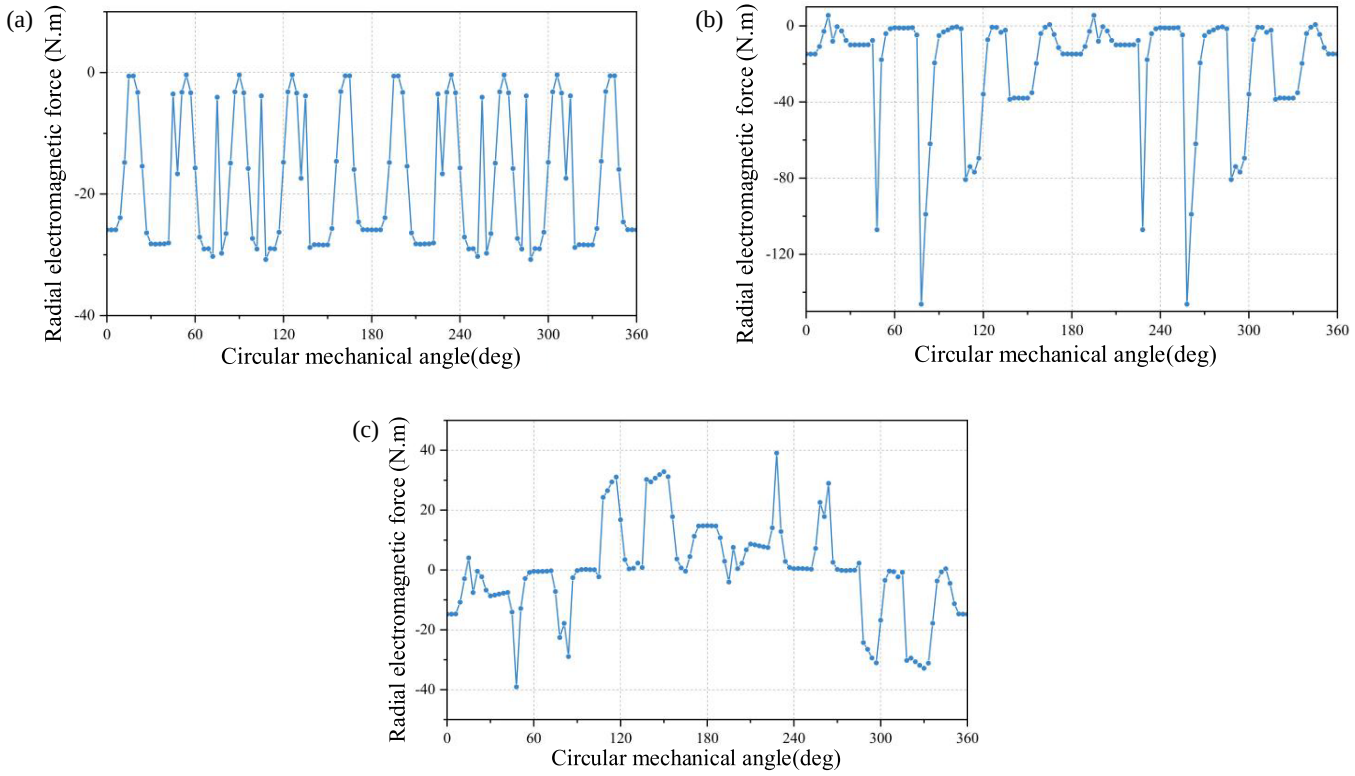

FIGURE 10. Radial electromagnetic force of the VLF-RSPM under different operating conditions: (a) No-load, (b) rated load, (c) weak-field high-speed.

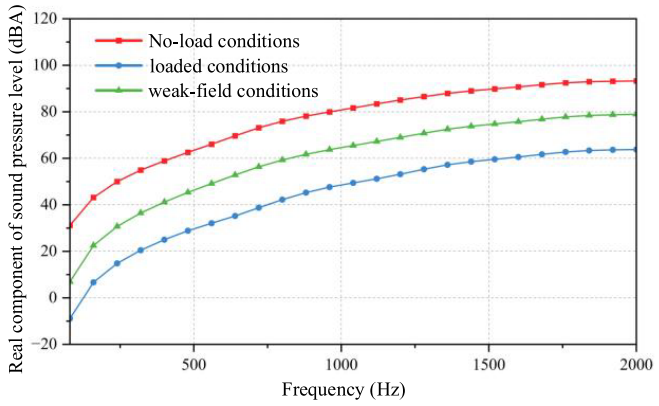

FIGURE 11. Noise frequency response of the VLF-RSPM under different operating conditions.

(2) High-order radial electromagnetic force harmonics: Dominate vibrations under weak-field, high-speed operating conditions;

(3) Fundamental radial electromagnetic force: The fundamental excitation source for vibrations across all operating conditions.

Except for the first-order rigid-body mode, as the order of the elastic modes increases, the motor's natural frequency tends to increase accordingly. There is a significant difference between the motor's radial modal frequency and the low-order harmonic frequencies of the radial electromagnetic forces acting on the stator teeth; the motor's radial modal frequency is far greater than the low-order harmonic frequencies of the radial electromagnetic forces. Therefore, under rated normal operating conditions, the motor will not experience resonance issues caused by low-order electromagnetic forces.

Based on the modal analysis of the VLF-RSPM described above, this paper conducts a comparative analysis of the radial electromagnetic force wave characteristics of the motor at different operating points to further investigate the differences in its electromagnetic vibration characteristics under no-load, rated load, and weak-field high-speed conditions. The relevant electromagnetic performance of the VLF-RSPM under different operating conditions is shown in Table 6, and the radial electromagnetic force of the VLF-RSPM under these conditions is shown in Figure 10.

As shown in Figure 10(a), under no-load conditions, the motor air-gap magnetic field is established solely by the permanent magnet excitation. The radial electromagnetic force exhibits

TABLE 6. Electromagnetic performance of the VLF-RSPM under different operating conditions.

Operating conditions	Variation ranges Final value Rotational speed (rpm)	Average torque (N·m)
No-load conditions	1500	0
Rated operating conditions	1500	26.2
Low-magnetic-field conditions	6000	7.2

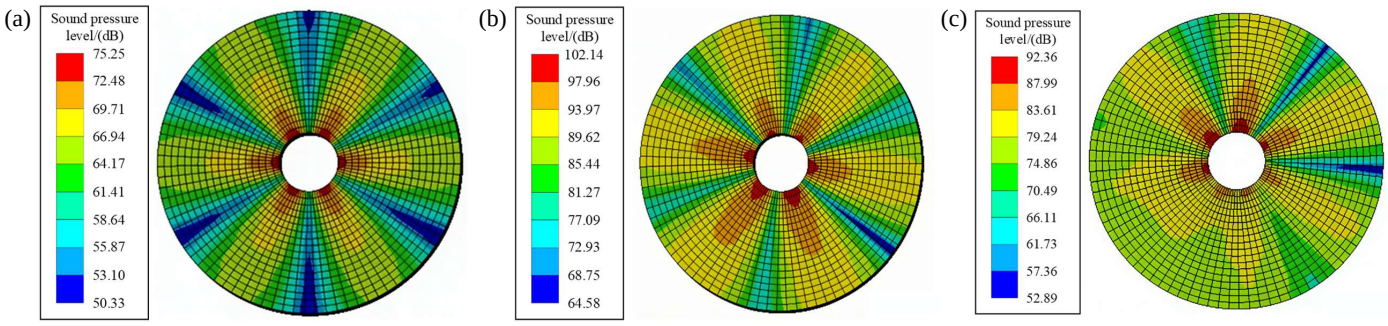

FIGURE 12. Sound pressure level contour plots of the VLF-RSPM under different operating conditions: (a) No-load, (b) rated load, (c) low-field, high-speed.

a regular spatial periodic distribution, with relatively low amplitude and uniform distribution, and a low content of higher-order harmonics, primarily manifesting as low-order spatial mode characteristics. As shown in Figure 10(b), under rated load conditions, the armature reaction field strongly couples with the permanent magnet field. The amplitude of the radial electromagnetic force increases significantly, and the degree of magnetic circuit saturation intensifies, causing distortion of the magnetic field waveform. When harmonic components approach the stator modal frequencies, structural resonance is induced. As shown in Figure 10(c), under high-speed weak-field operation, the motor applies a direct-axis demagnetizing current to weaken the air-gap magnetic field and achieve constant-power high-speed operation. The alternating frequency of the electromagnetic force wave significantly increases, and the high-frequency modulation effect caused by current harmonics and rotor motion intensifies, exciting high-order modal vibrations in the stator structure.

4.2. Noise Analysis

By calculating the radial electromagnetic force of the VLF-RSPM and coupling it with the entire motor, the harmonic response and vibration acceleration of the motor at different frequencies were obtained. The noise frequency response is shown in Figure 11, and the sound pressure level contour plots at different frequencies under various operating conditions are shown in Figure 12.

As shown in Figure 11, a distinct peak in sound pressure level occurs at the fundamental frequency under all three operating conditions. This is caused by the radial forces generated by the interaction between the fundamental component of the permanent magnet field and the fundamental component of the stator armature reaction.

As shown in Figure 12, under no-load conditions, the sound pressure level distribution is uniform and of low amplitude. The noise is dominated by low-order force waves from the permanent magnet field, with a simple frequency spectrum. The sound field exhibits axial symmetry, and end effects are not significant. Under rated operating conditions, the sound pressure level amplitude increases significantly. The coupling between armature reaction and the permanent magnet field causes radial electromagnetic force waves, stator vibration, and sound radiation efficiency to rise simultaneously, resulting in an asymmetric and more complex sound field distribution. Under weak-field high-speed operation, the sound pressure level exhibits high-speed characteristics; rotor windage and end-section airflow ripples make end-section noise more prominent, while the weak-field current in the main shaft induces high-frequency discrete noise peaks, producing a sharp electromagnetic screech.

4.3. Stress Analysis of Rotors

For the VLF-RSPM, the mechanical strength stability of the motor rotor is critical to the motor design in order to ensure the VLF-RSPM operates under high-speed conditions. In this paper, the strength of the motor rotor is verified using the Statics module on the VLF-RSPM model, as shown in Figure 13.

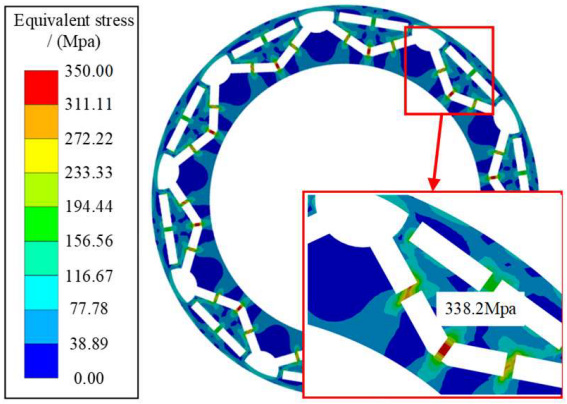

FIGURE 13. Equivalent stress on the rotor of the VLF-RSPM.

Figure 13 shows the simulation results of the VLF-RSPM rotor strength verification under high-speed weak-field operation, with a peak speed of 6000 r/min. The equivalent stress distribution shows that the maximum stress occurs at the magnetic bridge, reaching 338.2 MPa. This value is significantly lower than the 450 MPa yield strength of the silicon steel sheets; therefore, the equivalent stress distribution meets the yield strength requirements.

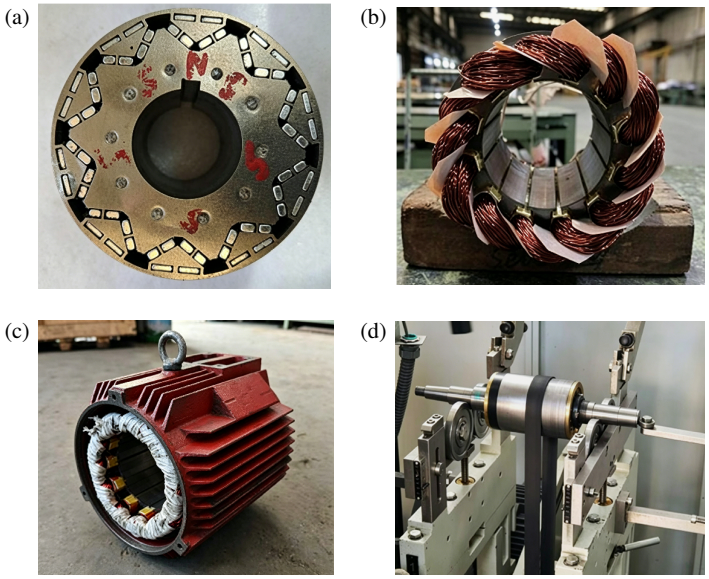

FIGURE 14. Motor prototype. (a) Rotor. (b) Stator. (c) Housing. (d) Shaft.

FIGURE 15. VLF-RSPM radial electromagnetic force wave test platform.

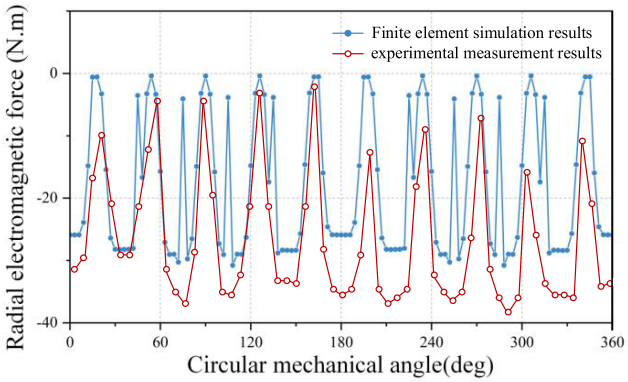

FIGURE 16. Results on radial electromagnetic force waves of the VLF-RSPM under no-load conditions.

5. VALIDATION OF RADIAL ELECTROMAGNETIC FORCE WAVE TESTING

To demonstrate the accuracy of the theoretical analysis in this paper and the feasibility of the optimized design, an experimental prototype, the VLF-RSPM, was constructed based on the results of the optimization design, as shown in Figure 14. The structures of the stator-rotor assembly, stator, housing, and shaft are shown in Figures 15(a) through (d), respectively. Figure 15 depicts the VLF-RSPM radial electromagnetic force wave testing platform, which is designed to enable precise measurement of the motor's no-load radial force.

Figure 16 compares the measured values of the radial electromagnetic force wave under no-load conditions for the VLF-RSPM with the finite element simulation results. Since the ideal finite element analysis did not account for manufacturing errors in the prototype or friction losses in the test platform, the minimum value of the radial electromagnetic force wave was $-38.2\,\mathrm{N{\cdot}m}$ in the experimental measurements, while the minimum value in the finite element simulation was $-30.8\,\mathrm{N{\cdot}m}$; However, the observed trend demonstrates the feasibility of the optimized design.

6. CONCLUSION

To address the issue of significant fluctuations in radial electromagnetic forces in variable-leakage-flux reverse-salient-pole permanent magnet synchronous motors (VLF-RSPMs), which make stable operation at high speeds challenging, this paper proposes a multi-objective hierarchical optimization design for VLF-RSPMs that incorporates vibration and noise suppression. This approach is based on an analysis of existing VLF-RSPMs and novel optimization methods. Through finite element analysis (FEA) and multiphysics coupling analysis, the following conclusions were reached:

(1) The multi-objective hierarchical optimization design addresses the issue that traditional optimization methods tend to overlook parameter ranges with high sensitivity, thereby strengthening the coupling between the optimization design of the VLF-RSPM and vibration and noise.

(2) Modal analysis, radial electromagnetic force analysis, noise analysis, and stress analysis of the optimized VLF-RSPM

demonstrate its operational reliability and suitability for high-speed operation.

(3) Finally, an experimental VLF-RSPM prototype and a radial electromagnetic force wave testing platform were designed. Experimental testing validated the accuracy of the theoretical analysis presented in this paper and the feasibility of the optimized design.

ACKNOWLEDGEMENT

This work was supported in part by the Youth Project of the Natural Science Foundation of Jiangxi Province (20242BAB20219), and in part by the Jiangxi Province Early Career Youth Science and Technology Talent Training Project (20244BCE52182).

REFERENCES

[1] Liu, X., J. Guo, R. Lu, Z. Liu, and B. Sun, "Design and analysis of a delta-shaped segmented variable leakage flux reverse-salient permanent magnet synchronous machine for electric vehicles," *Progress In Electromagnetics Research C*, Vol. 152, 197–208, 2025.

[2] Liu, X., H. Hu, Q. Jia, Z. Liu, and Z. Zhu, "Lower cost variable-leakage-flux reverse-salient-pole permanent magnet motor by reducing rare-earth permanent magnet usage," *Progress In Electromagnetics Research C*, Vol. 166, 57–67, 2026.

[3] Deng, W., S. Zuo, W. Chen, Z. Qian, C. Qian, and W. Cao, "Comparison of eccentricity impact on electromagnetic forces in internal- and external-rotor permanent magnet synchronous motors," *IEEE Transactions on Transportation Electrification*, Vol. 8, No. 1, 1242–1254, Mar. 2022.

[4] Liang, J., A. D. Callegaro, B. Bilgin, and A. Emadi, "A novel three-dimensional analytical approach for acoustic noise modeling in switched reluctance machines," *IEEE Transactions on Energy Conversion*, Vol. 36, No. 3, 2099–2109, Sep. 2021.

[5] Liang, W., J. Wang, P. C.-K. Luk, and W. Fei, "Analytical study of stator tooth modulation on electromagnetic radial force in permanent magnet synchronous machines," *IEEE Transactions on Industrial Electronics*, Vol. 68, No. 12, 11 731–11 739, Dec. 2021.

[6] Zhu, Z. Q., Z. P. Xia, L. J. Wu, and G. W. Jewell, "Analytical modeling and finite-element computation of radial vibration force in fractional-slot permanent-magnet brushless machines," *IEEE Transactions on Industry Applications*, Vol. 46, No. 5, 1908–1918, Sep.-Oct. 2010.

[7] Liu, F., X. Wang, H. Wei, L. Xiong, and X. Zhang, "Prediction of electromagnetic performance for IPMSM based on improved analytical model considering saturation effects," *IEEE Transactions on Transportation Electrification*, Vol. 10, No. 1, 1128–1144, Mar. 2024.

[8] Yan, B., X. Li, X. Wang, Y. Yang, and D. Chen, "Magnetic field prediction for line-start permanent magnet synchronous motor via incorporating geometry approximation and finite difference method into subdomain model," *IEEE Transactions on Industrial Electronics*, Vol. 70, No. 3, 2843–2854, Mar. 2023.

[9] Zhou, H., X. Wang, W. Zhao, J. Liu, Z. Xing, and Y. Peng, "Rapid prediction of magnetic and temperature field based on hybrid subdomain method and finite-difference method for the interior permanent magnet synchronous motor," *IEEE Transactions on Transportation Electrification*, Vol. 10, No. 3, 6634–6651, Sep. 2024.

[10] An, Y., C. Ma, N. Zhang, Y. Guo, M. Degano, C. Gerada, F. Bu, X. Yin, Q. Li, and S. Zhou, "Calculation model of armature reaction magnetic field of interior permanent magnet synchronous motor with segmented skewed poles," *IEEE Transactions on Energy Conversion*, Vol. 37, No. 2, 1115–1123, Jun. 2022.

[11] Peng, C., D. Wang, B. Wang, J. Li, C. Xu, and X. Wang, "Torque ripple and electromagnetic vibration suppression in permanent magnet synchronous motor using segmented rotor with different pole widths," *IEEE Transactions on Magnetics*, Vol. 58, No. 9, 1–5, Sep. 2022.

[12] Lu, Y., J. Li, R. Qu, D. Ye, H. Lu, J. Sun, M. Ge, and H. Xu, "Electromagnetic force and vibration analysis of permanent-magnet-assisted synchronous reluctance machines," *IEEE Transactions on Industry Applications*, Vol. 54, No. 5, 4246–4256, Sep.–Oct. 2018.

[13] Liu, X., Z. Zhao, W. Jia, Y. Ji, D. Fu, and H. Qiu, "Electromagnetic vibration reduction of a magnetic induction modulated permanent magnet synchronous linear motor," *IEEE Transactions on Transportation Electrification*, Vol. 12, No. 1, 566–577, Feb. 2026.

[14] Yin, H., W. Hua, Z. Wu, and H. Zhang, "Fourier-based vibration model of electrical machines considering nonideal orthogonality between electromagnetic forces and structural modes," *IEEE Transactions on Industrial Electronics*, Vol. 71, No. 5, 4485–4494, May 2024.

[15] Zhu, X., W. Wu, L. Quan, Z. Xiang, and W. Gu, "Design and multi-objective stratified optimization of a less-rare-earth hybrid permanent magnets motor with high torque density and low cost," *IEEE Transactions on Energy Conversion*, Vol. 34, No. 3, 1178–1189, Sep. 2019.

[16] Bonthu, S. S. R., S. Choi, and J. Baek, "Design optimization with multiphysics analysis on external rotor permanent magnet-assisted synchronous reluctance motors," *IEEE Transactions on Energy Conversion*, Vol. 33, No. 1, 290–298, Mar. 2018.

[17] Liu, L., Y. Guo, G. Lei, W. Yin, and J. Zhu, "Multi-objective design optimization of an IPMSM drive system based on loss minimization control strategy," in *2023 IEEE International Magnetic Conference — Short Papers (INTERMAG Short Papers)*, 1–2, Sendai, Japan, 2023.

[18] Lei, G., C. Liu, J. Zhu, and Y. Guo, "Techniques for multilevel design optimization of permanent magnet motors," *IEEE Transactions on Energy Conversion*, Vol. 30, No. 4, 1574–1584, Dec. 2015.

[19] Song, J., F. Dong, J. Zhao, H. Wang, Z. He, and L. Wang, "An efficient multiobjective design optimization method for a PMSLM based on an extreme learning machine," *IEEE Transactions on Industrial Electronics*, Vol. 66, No. 2, 1001–1011, Feb. 2019.

[20] Deng, W. and S. Zuo, "Axial force and vibroacoustic analysis of external-rotor axial-flux motors," *IEEE Transactions on Industrial Electronics*, Vol. 65, No. 3, 2018–2030, Mar. 2018.

[21] Deng, W. and S. Zuo, "Comparative study of sideband electromagnetic force in internal and external rotor PMSMs with SVPWM technique," *IEEE Transactions on Industrial Electronics*, Vol. 66, No. 2, 956–966, Feb. 2019.